

Quantification of spin-charge interconversion in highly resistive sputtered $\text{Bi}_x\text{Se}_{1-x}$ with nonlocal spin valves

Isabel C. Arango ^{1,*,\dagger} Won Young Choi ^{1,*} Van Tuong Pham ² Inge Groen ¹ Diogo C. Vaz ¹
 Punyashloka Debashis,⁴ Hai Li ⁴ Mahendra DC ⁴ Kaan Oguz ⁴ Andrey Chuvilin ^{1,3} Luis E. Hueso ^{1,3}
 Ian A. Young,⁴ and Fèlix Casanova ^{1,3,\ddagger}

¹*CIC nanoGUNE BRTA, 20018 Donostia-San Sebastián, Basque Country, Spain*

²*IMEC, Kapeldreef 75, 3001 Leuven, Belgium*

³*IKERBASQUE, Basque Foundation for Science, 48009 Bilbao, Basque Country, Spain*

⁴*Components Research, Intel Corporation, Hillsboro, Oregon 97124, USA*



(Received 12 July 2023; accepted 8 September 2023; published 28 September 2023)

The development of spin-orbitronic devices, such as magnetoelectric spin-orbit logic devices, calls for materials with a high resistivity and a high spin-charge interconversion efficiency. One of the most promising candidates in this regard is sputtered $\text{Bi}_x\text{Se}_{1-x}$. Although there are several techniques to quantify spin-charge interconversion, reported values to date for sputtered $\text{Bi}_x\text{Se}_{1-x}$ have often been overestimated due to spurious effects related to local currents combined with a lack of understanding of the effect of the interfaces and the use of approximations for unknown parameters, such as the spin diffusion length. In the present study, nonlocal spin valves are used to inject pure spin currents into $\text{Bi}_x\text{Se}_{1-x}$, allowing us to directly obtain its spin diffusion length as well as its spin Hall angle, from 10 K up to 300 K. These values, which are more accurate than those previously reported in sputtered $\text{Bi}_x\text{Se}_{1-x}$, evidence that the efficiency of this material is not exceptional. Indeed, the figure of merit for spin-charge interconversion, given by the product of these two parameters, is slightly under 1 nm. Our work demonstrates the importance of considering all material parameters and interfaces when quantifying the spin transport properties of materials with strong spin-orbit coupling.

DOI: [10.1103/PhysRevB.108.104425](https://doi.org/10.1103/PhysRevB.108.104425)

I. INTRODUCTION

Moore's 1965 prediction on the downscaling of transistor prediction [1,2] has held strong for a remarkable amount of time. However, the complementary metal-oxide-semiconductor (CMOS) technology on which it has relied thus far is now reaching its scaling limits, sparking an intense effort [3] to find alternative approaches with new functionalities that can be integrated in the next generation of electronic devices. One of these approaches, known as spintronics, makes use of the electron's spin degree of freedom in non-volatile memories [4,5] and logic devices [6–8]. Spintronics relies on materials with strong spin-orbit coupling (SOC), which allow spin-charge interconversion (SCI) via the spin Hall effect (SHE) [9] or the Edelstein effect [10]. A recent proposal in the field introduced a device concept known as magnetoelectric spin-orbit (MESO) [8,11] for logic operations based on one device with two different nodes cascading multiple devices. The input node is used to write a magnetic element with voltage using magnetoelectric effects and the output node to read the magnetic state of the element with spin-to-charge conversion [12]. One of the requirements for MESO is that the readout voltage should be above the coercive voltage of the magnetoelectric material (~ 100 mV) to drive

the next element in a logic operation, a value which could be reached by using materials with high SCI efficiencies and high resistivities [13].

In this regard, one promising candidate for the readout node of the MESO device is Bi_2Se_3 , which has been reported to have both high SCI efficiency and high resistivity [14,15]. Bi_2Se_3 is well known as a topological insulator [16]. This class of materials shows spin-momentum locking at the topologically protected surface states, a feature that allows an efficient Edelstein effect (characterized by the inverse Edelstein length, λ_{IEE}). Exploitation of these surface states typically requires an epitaxial structure and low temperature to minimize bulk conduction [17,18]. Recently, however, some works [19–23] reported large SCI even at room temperature in polycrystalline $\text{Bi}_x\text{Se}_{1-x}$ (BiSe) grown by sputtering, a simple technique compatible with the industrial processes. Although the Edelstein effect is the source of SCI in ideal topological insulators, many works use the spin Hall angle (θ_{SH}) to quantify the SCI efficiency in this class of materials [24]. In this case, just like for materials exhibiting SHE, the spin diffusion length (λ_s) is an essential parameter for a proper quantification of the SCI efficiency. Indeed, for many applications including MESO, the relevant figure of merit is the $\theta_{\text{SH}}\lambda_s$ product [13], which is equivalent to λ_{IEE} [25]. However, λ_s for sputtered BiSe is usually taken from few reports describing epitaxially grown Bi_2Se_3 [26–29], which not only has a different crystal structure, but also a different composition. This dissimilarity invariably leads to inaccuracies in the subsequent

*These authors contributed equally to this work.

^{\dagger}i.arango@nanogune.eu

^{\ddagger}f.casanova@nanogune.eu

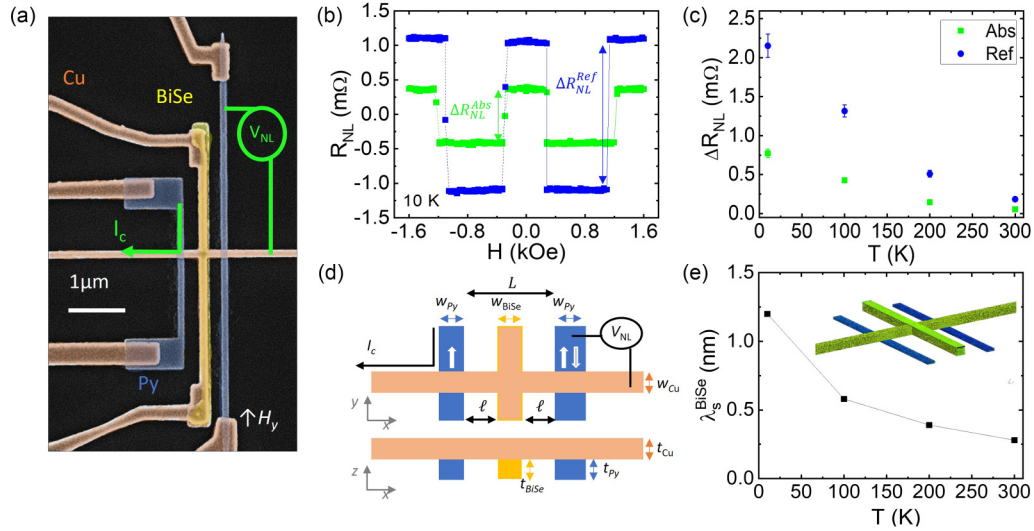


FIG. 1. (a) Top-view SEM image of the LSV device with the ferromagnetic Py electrodes (blue), the BiSe wire in between (yellow), and the Cu spin transport channel (orange). The electrical configuration for the spin absorption measurement is shown in green. (b) Nonlocal resistance R_{NL} as a function of the external magnetic field for the reference LSV (blue curve) and the LSV with the BiSe wire (green curve) at 10 K. The corresponding spin signals are indicated by arrows. (c) Spin signals as a function of temperature for the reference LSV and the LSV with the BiSe wire. (d) Schematic representation of the LSV with the BiSe wire showing the geometrical parameters in the top view (upper part) and cross-sectional view (bottom part). The ferromagnetic electrodes are separated by a distance $L = 650$ nm. (e) Spin diffusion length of BiSe, λ_s^{BiSe} , as a function of the temperature, extracted from the data in (c) through a 3D FEM analysis. In the 3D FEM simulation, the resistivity of the Ti layer between Cu and BiSe is set to be $50 \mu\Omega\text{cm}$. Inset: Geometry and mesh of the 3D FEM model.

quantification of the SCI efficiency of BiSe. In addition, most SCI quantification techniques require the SCI material to be in direct contact with a ferromagnetic or transition metal, but recent studies on Bi_2Se_3 have reported interdiffusion by solid-state reaction when it is in contact with metals [30–34]. Thus, a new layer forms at the interface through which the spins are injected or pumped, making an accurate quantification of the spin properties (λ_s and θ_{SH}) of this material difficult [31,34].

In this paper, we characterize sputtered BiSe through the spin absorption technique using lateral spin valves (LSVs) and two separate measurement configurations [35–38]. This nonlocal method allows us to independently quantify the spin diffusion length (λ_s^{BiSe}) and the spin Hall angle ($\theta_{\text{SH}}^{\text{BiSe}}$) of BiSe. The use of a nonlocal measurement avoids spurious effects related to local currents, such as Oersted fields in spin-orbit torque techniques or fringe-field-induced voltages in three-terminal potentiometric techniques [39]. Furthermore, in order to reduce interdiffusion, we grow the metals in contact with the BiSe wire by *e*-beam evaporation, a gentler deposition technique than sputtering. A much better quality of the device interface is confirmed by transmission electron microscopy (TEM) and elemental analysis characterization. This information allows us to model our devices and perform a three-dimensional finite element method (3D FEM) analysis to extract the spin transport parameters at different temperatures. The SCI efficiency, characterized by the $\theta_{\text{SH}}^{\text{BiSe}}\lambda_s^{\text{BiSe}}$ product, is found to be up to 0.92 nm at 100 K, and 0.63 nm at room temperature. Our work highlights the importance of considering all the details of BiSe and its interfaces for a proper quantification of the spin transport properties of this material.

II. EXPERIMENTAL DETAILS

A. Device fabrication

All LSV devices were fabricated on Si/SiO₂ (150 nm) substrates [see Fig. 1(a)]. Three electron-beam lithography (eBL) steps are needed for the complete fabrication of the LSVs. The first step is used to define the ferromagnetic wires: we spin-coated the substrates using ZEP (methyl styrene and chloromethyl acrylate copolymer) as a positive resist, patterned it by eBL, deposited 30 nm of Py ($\text{Ni}_{81}\text{Fe}_{19}$) by *e*-beam evaporation (base pressure of 2×10^{-9} Torr, rate of 0.6 \AA/s), and performed the liftoff process. To remove possible sidewalls on the wires after the liftoff, we Ar-ion milled the sample at an angle of 10° with respect to the substrate plane and an acceleration voltage of 50 V. The second step defines the BiSe wires: we spin-coated a double layer of PMMA (polymethyl methacrylate), patterned it by eBL, deposited 10 nm of BiSe by sputtering at room temperature, using a target of stoichiometric Bi_2Se_3 (99.999% purity) in a UHV sputtering system with a base pressure of 3×10^{-8} Torr. Bi_2Se_3 was sputtered at 35 W rf power and 3 mTorr Ar pressure, yielding a deposition rate of 0.09 \AA/s . Subsequently, the wires were capped *in situ* with 2 nm of Pt (80 W DC at 3 mTorr Ar pressure) and liftoff was performed. The third step defines the Cu spin transport channel: we used a double layer of PMMA, patterned it with eBL, and then used Ar-ion milling to remove the Pt capping and clean the surfaces of the Py wires. We then transferred the sample to the UHV evaporation system to grow 2 nm of Ti by *e*-beam evaporation (at a rate of 0.2 \AA/s), followed by 100 nm of Cu *in situ* by thermal evaporation at a rate of 1.5 \AA/s . The Ti layer is added to help the Cu grow on top of BiSe (see Supplemental Material S1 [40]).

and acts as an interface between the Cu channel and the Py and BiSe electrodes. Liftoff was then performed. Finally, the entire sample was capped by sputtering 5 nm of SiO₂ (200 W rf at 3 mTorr of Ar).

B. Transport measurements

Transport measurements were performed in a Quantum Design Physical Properties Measurement System (PPMS), using the “DC reversal” technique with a Keithley 2182 nanovoltmeter and a 6221 current source. Thermoelectric effects arising from Joule heating are removed with the use of the “DC reversal” technique [41].

C. TEM characterization

Cross-sectional samples for analysis by scanning transmission electron microscopy with energy dispersive x-ray spectroscopy (STEM-EDX) were prepared from tested devices by the standard focused ion beam (FIB) lamella preparation method: the surface of the deposited samples was first protected by ion beam Pt deposition, the lamellas were cut and lifted onto a Cu three-post half grid. Cross sections were studied on a Titan 60–300 TEM (FEI, Netherlands) at 300 kV in STEM mode. EDX spectral images were obtained using an EDAX RTEM spectrometer. Element distribution maps were obtained by multiple linear least squares (MLLS) fitting of experimental spectra using simulated spectral components.

III. RESULTS AND DISCUSSION

A. Lateral spin valves

In a reference LSV without the BiSe wire, a charge current (I_C) is injected from one of the ferromagnetic Py electrodes into the nonmagnetic Cu channel, creating a spin accumulation at the interface. These spins diffuse as a pure spin current (I_s) through the Cu channel with a characteristic diffusion length (λ_s^{Cu}) and is detected by the second Py electrode as a nonlocal voltage (V_{NL}). The nonlocal resistance R_{NL} is defined as the V_{NL} normalized to I_C . An external magnetic field is applied along the easy axis of the ferromagnet ($\pm y$ direction) to control the reversal of the magnetization of the two Py electrodes. The value of R_{NL} changes sign when the magnetization configuration of the two Py electrodes switches from parallel (R_{NL}^{P}) to antiparallel ($R_{\text{NL}}^{\text{AP}}$). The difference between these two configurations ($\Delta R_{\text{NL}}^{\text{Ref}} = R_{\text{NL}}^{\text{P}} - R_{\text{NL}}^{\text{AP}}$) allows us to obtain the spin signal by removing any baseline arising from non-spin-related effects.

In a similar LSV device, we place a BiSe wire between the two Py electrodes [Fig. 1(a)]. Part of the spin current diffusing along the Cu channel will be absorbed in the BiSe wire and, thus, the spin signal picked up by the Py detector, $\Delta R_{\text{NL}}^{\text{Abs}}$, will be smaller than $\Delta R_{\text{NL}}^{\text{Ref}}$ [see Fig. 1(b)]. The Ti/Cu cross is deposited on top of the BiSe wire to improve the electrical contact due to the high resistivity of this material [31], and to help us perform spin-to-charge conversion measurements on the same device (see below). Figure 1(c) plots the values of $\Delta R_{\text{NL}}^{\text{Ref}}$ and $\Delta R_{\text{NL}}^{\text{Abs}}$ at different temperatures (T) between 10 and 300 K. The decrease of the spin signals with increasing T is expected because λ_s^{Cu} decreases with temperature (Ref. [42]

and Supplemental Material S3 [40]) and less spin current reaches the ferromagnetic detector.

To extract the spin diffusion length of BiSe (λ_s^{BiSe}) from the spin absorption measurement, we performed a 3D FEM simulation using the following: (i) the experimental resistivities for all materials (Supplemental Material S2 [40]); (ii) the interface spin polarization (α_I) of the Py/Ti and λ_s^{Cu} of the Cu channel, obtained from reference LSVs with different electrode distances (L) by fitting the spin signals ΔR_{NL} vs L using the 1D spin diffusion model (see Supplemental Material S3 [40]); (iii) the contact resistance of the Py/Ti/Cu interface extracted from an interface resistance measurement with four probe configuration (Supplemental Material S4 [40]); (iv) the measured spin signal after absorption ($\Delta R_{\text{NL}}^{\text{Abs}}$). Besides λ_s^{BiSe} , the only unknown parameter in the 3D FEM simulation is the resistivity of the Ti layer (ρ_{Ti}) between Cu and BiSe. Unfortunately, due to our device geometry, with the Ti layer sandwiched between the Cu channel and the BiSe wire, it is not possible to directly extract ρ_{Ti} . Therefore, we estimate this resistivity in a separate experiment described in Supplemental Material S5 [40], from which we obtain the value 50 $\mu\Omega\text{cm}$. As described in Supplemental Material S6 [40], we extracted λ_s^{BiSe} at different temperatures, as shown in Fig. 1(e). The extracted value is in all cases of the order of or smaller than 1 nm, reaching 0.28 nm at room temperature. This value is significantly smaller than the values of 1.6–6.2 nm previously reported for epitaxially grown Bi₂Se₃ [26,27].

B. Spin-charge interconversion

In the same device used to performed the spin absorption measurement, we measure the inverse spin Hall effect (ISHE) using a different electrical configuration [see sketch in Fig. 2(a)]. This time, we inject a charge current (I_C) from one of the Py electrodes into the Cu channel while applying an in-plane magnetic field along the hard axis of Py (x direction). An x -polarized spin current is created and reaches the BiSe wire, where it is partially absorbed in the z direction and converted into a charge current (I_{ISHE}) along the y direction [Fig. 2(c)]. This charge current is detected as a voltage (V_{ISHE}) along the BiSe wire (shunted by Cu) under open-circuit conditions. The ISHE resistance ($R_{\text{ISHE}} = V_{\text{ISHE}}/I_C$) is measured by sweeping the external magnetic field along the x direction. By reversing the field, the opposite R_{ISHE} is obtained [see Fig. 2(d)], because the Py magnetization changes direction and, thus, so does the spin polarization of the spin current. The difference between the two R_{ISHE} values at saturation is denoted as the ISHE signal ($2\Delta R_{\text{ISHE}}$) and allows removing any background signal. Indeed, the combination of Seebeck and Peltier effects can give rise to a baseline in the nonlocal signal because they are linear with the applied current, as explained in Ref. [43]. However, this contribution is removed by taking the difference between the two values at saturation. Since the material we study is not magnetic, a spurious contribution due to the combination of Peltier effect and anomalous Nernst effect as the one observed in the Weyl ferromagnet Co₂MnGa [44] is not present in our case.

As shown in Fig. 2(b), it is possible to obtain the direct SHE by swapping the current and voltage probes (i.e., applying the charge current in the BiSe wire and measuring

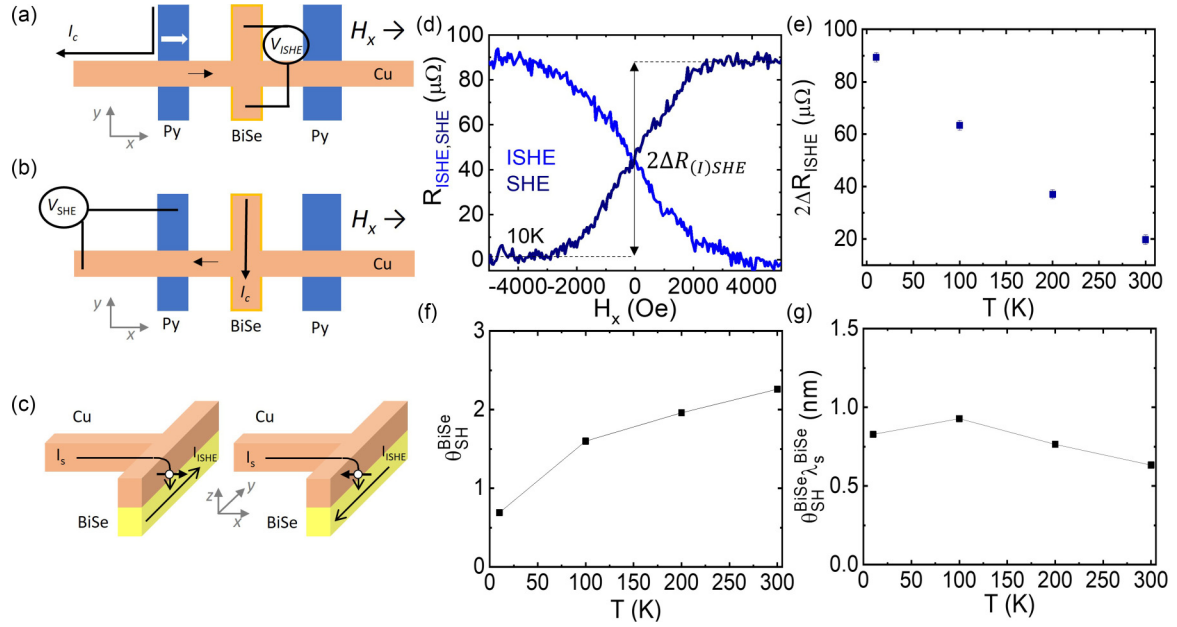


FIG. 2. Schematic representation of the LSV with the middle wire showing (a) spin-to-charge (ISHE) and (b) charge-to-spin (SHE) conversion measurement configurations. (c) After the spin injection from the Py (blue) to the Cu spin transport channel (orange) in (a) the spin current flows (with a spin polarization in the $+x$ direction) along the Cu channel and is absorbed by the BiSe wire (yellow) along the $-z$ direction. Due to the ISHE, the spin current is converted into a charge current (I_{ISHE}) in the $+y$ direction (left sketch). If the magnetic field is reversed, the spin polarization of the spin current also reverses ($-x$ direction) as does the converted I_{ISHE} ($-y$ direction) (right sketch), which is detected as an open-circuit voltage. (d) ISHE (R_{ISHE}) and SHE (R_{SHE}) resistances as function of the external magnetic field at 10 K. The corresponding (I)SHE signal is indicated by an arrow. (e) ISHE signal ($2\Delta R_{\text{ISHE}}$) as a function of temperature. (f) Spin Hall angle of BiSe ($\theta_{\text{SH}}^{\text{BiSe}}$) extracted from the data in (e) and a 3D FEM analysis, considering a Ti resistivity of $50 \mu\Omega\text{cm}$. (g) $\theta_{\text{SH}}^{\text{BiSe}} \lambda_s^{\text{BiSe}}$ product as a function of temperature.

the output voltage between the Py electrode and the Cu channel). Both SHE and ISHE resistance curves have the same amplitude but opposite sign [$R_{\text{ISHE}}(H) = R_{\text{SHE}}(-H)$], see Fig. 2(d)], as expected from Onsager's reciprocity [45,46]. The (I)SHE signals decrease with increasing T , as shown in Fig. 2(e). To extract the spin Hall angle ($\theta_{\text{SH}}^{\text{BiSe}}$) from the ISHE measurement, we performed a 3D FEM simulation using the same geometry (dimensions) and material parameters as before, plus the λ_s^{BiSe} value obtained in the very same device (see Supplemental Material S7 [40]). Figure 2(f) shows the $\theta_{\text{SH}}^{\text{BiSe}}$ values extracted as a function of T (from 0.69 at 10 K to 2.26 at 300 K). These values are more accurate than those previously reported in sputtered BiSe because of the knowledge of λ_s^{BiSe} . As a control experiment, we measured the reference device (without the BiSe) with the direct spin Hall configuration. As expected, no signal is observed (see Supplemental Material S8 [40]).

The product $\theta_{\text{SH}}^{\text{BiSe}} \lambda_s^{\text{BiSe}}$, which is the figure of merit for the efficiency of a MESO device, is shown in Fig. 2(g) as a function of T . $\theta_{\text{SH}}^{\text{BiSe}} \lambda_s^{\text{BiSe}}$ does not change significantly with T , having values between 0.63 and 0.92 nm, slightly higher than the prototypical heavy metals [13,35,47,48].

C. Transmission electron microscopy

After the magnetotransport characterization (spin absorption and spin Hall measurements), we characterized the device cross sections by TEM/STEM imaging combined with EDX analysis with particular emphasis on materials interfaces.

Interfaces play a key role in spintronic and spin-orbitronic devices, since they can enhance or reduce the efficiency of the spin current injection in SCI experiments [33,34,49–53]. Figure 3(a) shows a cross-sectional view of the LSV. The two Py electrodes (spin injector and detector) can be observed at the right and left of the image with the 10-nm-thick BiSe wire between them. They are covered by a homogeneous 2-nm-thick Ti layer followed by the 100-nm-thick Cu channel. The chemical distribution has been characterized by EDX. Figure 3(b) shows the different elemental maps for the elements of interest obtained by EDX in the region indicated by the orange rectangle in Fig. 3(a) (see the additional information in Supplemental Material S9 [40]). The elemental maps evidence that the 2-nm-thick Ti buffer layer is oxidized throughout the device. Figure 3(d) shows a higher resolution image of the area defined by the blue rectangle in Fig. 3(c): the chemical distribution of Bi and Se within the BiSe wire evidences that the two elements are not homogeneously distributed and suggests diffusion has taken place inside the wire. A universal characterization of sputtered BiSe may become difficult due to the unavoidable fact that it is a highly reactive material in contact with other metallic materials. Figure 3(e) shows a high-resolution TEM image of the same wire [red rectangle in Fig. 3(c)], where the polycrystalline and granular structure of the BiSe layer can be observed. In some grains alternating Bi_2Se_3 quintuple layers and Bi bilayers are visible, in agreement with a previous report [31]. The layer of Ti on top of BiSe can be clearly distinguished and shows an amorphous morphology. Since, after Ar-ion milling, the Ti

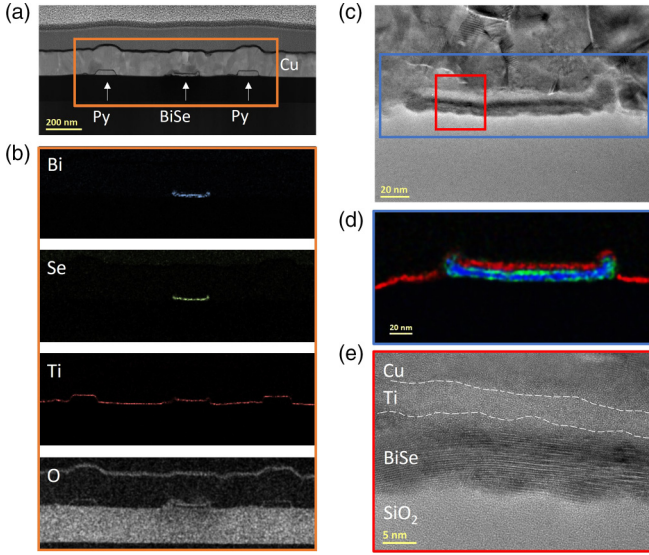


FIG. 3. (a) Cross-sectional TEM image of the LSV device. The orange rectangle indicates the area where EDX analysis was performed. (b) EDX analysis of the cross section of the LSV [orange rectangle in (a)], showing the elements of interest in each subpanel: Bi (blue), Se (green), Ti (red), and O (grey). (c) Cross-sectional TEM image of the BiSe wire inside the LSV. (d) Color-coded elements image corresponding to the area marked with a blue rectangle in (c). (e) High resolution TEM image corresponding to the red rectangle area in (c).

and then the Cu spin transport channel are deposited *ex situ* by *e*-beam evaporation, the interface does not show a detectable interdiffusion, in contrast to what is reported by contacting BiSe with transition metals by sputter deposition (all *in situ*) [31,34] and molecular-beam-epitaxy-grown Bi_2Se_3 with metallic contacts deposited by *e*-beam evaporation [30].

D. TiO_x interface layer

In the 3D FEM simulations described above and performed for both spin absorption and spin Hall measurements, we considered a metallic Ti layer with $\rho_{\text{Ti}} = 50 \mu\Omega\text{cm}$, a value obtained from our control experiment (Supplemental Material S5 [40]). However, as pointed out in the previous section, our EDX analysis shows that the Ti layer in the LSV becomes

oxidized. Therefore, to obtain more accurate values of λ_s^{BiSe} and $\theta_{\text{SH}}^{\text{BiSe}}$, we need to account for the presence of oxygen by increasing the resistivity of Ti. As mentioned, our device geometry does not allow extraction of the resistivity of the Ti layer in contact with the BiSe, however since the Ti layer also covers the Py electrodes, we were able to measure the interface resistance at that junction using the four-probe configuration (Supplemental Material S4 [40]). Taking this value and calculating the resistivity for the 2-nm-thick oxidized Ti layer, we obtained $\rho_{\text{Ti}} \approx 1000 \mu\Omega\text{cm}$. The same material will grow differently on different materials and, therefore, we cannot directly assume that the resistivity of Ti on Py will be the same as that of Ti on BiSe, but we can take it as an upper limit. Repeating the 3D FEM simulation with ρ_{Ti} values from 50 to $1000 \mu\Omega\text{cm}$ (see Supplemental Material S10 [40]), we extracted λ_s^{BiSe} as a function of ρ_{Ti} , which is plotted in Fig. 4(a). At 10 K, for example, λ_s^{BiSe} varies between 1.1 and 2.7 nm. In order to rule out the possibility of a higher resistivities of the Ti layer, we also performed a simulation using $\rho_{\text{Ti}} = 1500 \mu\Omega\text{cm}$ (see Supplemental Material S10 [40]). In this case, λ_s^{BiSe} tends to infinity, that is, fewer spins can reach the BiSe layer, rendering the properties of this second layer irrelevant in the 3D model. We also performed a simulation considering the BiSe resistivity measured in the vertical direction (across the thickness) at 300 K by Choi *et al.* ($\rho_{\text{BiSe}} = 600 \mu\Omega\text{cm}$) [31] (see Supplemental Material S10 [40]), a much lower value compared to our own measured value at room temperature ($\rho_{\text{BiSe}} = 4100 \mu\Omega\text{cm}$; see Supplemental Material S2 [40]). Comparison of the extracted spin diffusion length for the simulations using our measured values of ρ_{BiSe} [see Fig. 4(a), blue, black, red, and light green curves] shows λ_s^{BiSe} to be relatively small in all cases, and to decrease with increasing temperature for any ρ_{Ti} . However, comparing λ_s^{BiSe} at room temperature (light green and dark cyan curves) and ρ_{Ti} lower than $100 \mu\Omega\text{cm}$, we find that the low BiSe resistivity value (\sim six times smaller) yields a spin diffusion length more than three times larger than the one obtained using our higher value ($\rho_{\text{BiSe}} = 4100 \mu\Omega\text{cm}$).

We additionally performed a 3D FEM simulation (see Supplemental Material S11 [40]) to extract the conversion efficiency ($\theta_{\text{SH}}^{\text{BiSe}}$), using the new values of λ_s^{BiSe} for each value of ρ_{Ti} from 50 to $1000 \mu\Omega\text{cm}$. Our simulation results for $\theta_{\text{SH}}^{\text{BiSe}}$ as a function of ρ_{Ti} are plotted in Fig. 4(b). As an example, the value at 10 K varies between 0.54 and 0.88. We also

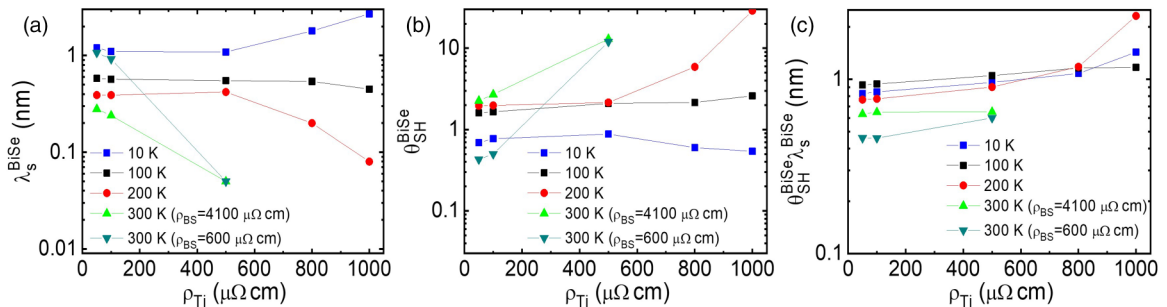


FIG. 4. (a) Spin diffusion length λ_s^{BiSe} , (b) spin Hall angle $\theta_{\text{SH}}^{\text{BiSe}}$, and (c) the $\theta_{\text{SH}}^{\text{BiSe}} \lambda_s^{\text{BiSe}}$ product extracted from the 3D FEM analysis as a function of the Ti resistivity (ρ_{Ti}) at different temperatures, from 10 K up to 300 K. Additionally, at 300 K, we also use a lower resistivity of BiSe reported in Ref. [31].

TABLE I. Summary of ρ_{BiSe} , λ_s^{BiSe} , $\theta_{\text{SH}}^{\text{BiSe}}$, λ_{IEE} values obtained in this work and in previous reports on sputtered BiSe.

	t_{BiSe} (nm)	T (K)	ρ_{BiSe} ($\mu\Omega\text{cm}$)	λ_s^{BiSe} (nm)	$\theta_{\text{SH}}^{\text{BiSe}}$	λ_{IEE} (nm)	Method
Bi _x Se _{1-x} (this work)	10	10	6200	1.09–2.70	0.54–0.88	0.82–1.46 ^a	nonlocal device (LSV)
		100	5900	0.45–0.58	1.60–2.61	0.92–1.17 ^a	
		200	5100	0.08–0.39	1.96–28.90	0.76–2.31 ^a	
		300	4100	0.05–0.28	2.26–13.01	0.63–0.65 ^a	
		300	600 ^b	0.05–1.07	0.43–11.99	0.46–0.60 ^a	
Bi _{0.5} Se _{0.5} /Ti [31]	2–16	300	600	0.5	0.45	0.225 ^a	local device (T shaped)
Bi _{0.45} Se _{0.55} /Pt [31]	3–5	300	3700	0.35	3.2	1.12 ^a	local device (T shaped)
Bi _x Se _{1-x} /CoFeB [19]	4–40	300	12820		18.62		harmonic Hall (DC)
Bi _x Se _{1-x} /YIG [21]	4–16	300				0.11	spin pumping
Bi _x Se _{1-x} /CoFeB [20]	2–16	300				0.32	spin pumping

$$^a\lambda_{\text{IEE}} \text{ (nm)} = \theta_{\text{SH}}^{\text{BiSe}} \lambda_s^{\text{BiSe}}.$$

^bValue taken from Ref. [31].

performed the simulation considering $\rho_{\text{BiSe}} = 600 \mu\Omega\text{cm}$ at 300 K (Supplemental Material S11 [40]). Finally, the product $\theta_{\text{SH}}^{\text{BiSe}} \lambda_s^{\text{BiSe}}$ as a function of ρ_{Ti} is shown in Fig. 4(c). Interestingly, this product does not present large variations with the resistivity of the interface layer, being fairly constant and generally lower than 1 nm. This indicates the robustness of this figure of merit in our analysis independently of the assumed resistivity of the interfacial Ti. Table I summarizes our results, taking the minimum and maximum values of these parameters for each temperature. Results from previous reports on sputtered BiSe are also included for comparison.

IV. CONCLUSIONS

We successfully injected a pure spin current into highly resistive sputtered BiSe using nonlocal spin valves and performed spin absorption measurements from 10 K up to room temperature. A 3D FEM analysis of the absorption data allowed us to extract the spin diffusion length λ_s^{BiSe} in this system. Spin-charge interconversion measurements were performed on the same device to extract the spin Hall angle $\theta_{\text{SH}}^{\text{BiSe}}$. From these two experiments, we were able to reliably obtain the $\theta_{\text{SH}}^{\text{BiSe}} \lambda_s^{\text{BiSe}}$ product, a relevant figure of merit characterizing SCI in MESO devices. Despite the uncertainty regarding the resistivity of the Ti layer separating the Cu spin channel and

the sputtered BiSe, the obtained values, generally lower than 1 nm, are robust. Although existing literature has reported a high SCI efficiency for BiSe and put this material forward as a promising candidate for MESO logic devices, our work shows otherwise. A more accurate characterization, relying on nonlocal devices that eliminate spurious effects, reveals that the SCI efficiency of sputtered BiSe is in fact too small to be used for MESO technology.

ACKNOWLEDGMENTS

This work was supported by Intel Corporation through the Semiconductor Research Corporation under MSR-INTEL TASK Grant No. 2017-IN-2744 and the “FEINMAN” Intel Science Technology Center, and by the Spanish Ministry of Science and Innovation (MICINN) (Project No. PID2021-122511OB-I00 and Maria de Maeztu Units of Excellence Programme No. CEX2020-001038-M). W.Y.C. acknowledges postdoctoral fellowship support from “Juan de la Cierva—Formación” Programme by the Spanish MICINN (Grant No. FJC2018-038580-I). D.C.V. acknowledges funding from the European Union’s Horizon 2020 Research and Innovation Programme under the Marie Skłodowska-Curie Grant No. 892983-SPECTER.

- [1] G. E. Moore, Cramming more components onto integrated circuits, *Proc. IEEE* **86**, 82 (1998).
- [2] R. Dennard, F. Gaensslen, W.-N. Yu, L. Rideout, E. Bassous, and A. Le Blanc, Design of ion-implanted small MOSFET’S dimensions with very, *IEEE J. Solid State Circuits* **9**, 257 (1974).
- [3] P. Barla, V. K. Joshi, and S. Bhat, Spintronic devices: A promising alternative to CMOS devices, *J. Comput. Electron.* **20**, 805837 (2021).
- [4] S. Bhatti, R. Sbiaa, A. Hirohata, H. Ohno, S. Fukami, and S. N. Piramanayagam, Spintronics based random access memory: A review, *Mater. Today* **20**, 530 (2017).
- [5] Q. Shao, P. Li, L. Liu, H. Yang, S. Fukami, A. Razavi, H. Wu, K. Wang, F. Freimuth, Y. Mokrousov *et al.*, Roadmap of spin-orbit torques, *IEEE Trans. Magn.* **57**, 1 (2021).
- [6] H. Dery, P. Dalal, Cywiński, and L. J. Sham, Spin-based logic in semiconductors for reconfigurable large-scale circuits, *Nature (London)* **447**, 573 (2007).
- [7] B. Behin-Aein, D. Datta, S. Salahuddin, and S. Datta, Proposal for an all-spin logic device with built-in memory, *Nat. Nanotechnol.* **5**, 266 (2010).
- [8] S. Manipatruni, D. E. Nikonov, C.-C. Lin, T. A. Gosavi, H. Liu, B. Prasad, Y.-L. Huang, E. Bonturim, R. Ramesh, and I. A. Young, Scalable energy-efficient magnetoelectric spin-orbit logic, *Nature (London)* **565**, 35 (2018).
- [9] J. Sinova, S. O. Valenzuela, J. Wunderlich, C. H. Back, and T. Jungwirth, Spin Hall effects, *Rev. Mod. Phys.* **87**, 1213 (2015).

- [10] H. Isshiki, P. Muduli, J. Kim, K. Kondou, and Y. C. Otani, Phenomenological model for the direct and inverse Edelstein effects, *Phys. Rev. B* **102**, 184411 (2020).
- [11] H. Li, C. C. Lin, D. E. Nikonov, and I. A. Young, Differential electrically insulated magnetoelectric spin-orbit logic circuits, *IEEE J. Explor. Solid-State Comput. Devices Circuits* **7**, 18 (2021).
- [12] D. C. Vaz *et al.*, Voltage-based magnetization switching and reading in magnetoelectric spin-orbit nanodevices, [arXiv:2302.12162](https://arxiv.org/abs/2302.12162).
- [13] V. T. Pham *et al.*, Spin-orbit magnetic state readout in scaled ferromagnetic/heavy metal nanostructures, *Nat. Electron.* **3**, 309 (2020).
- [14] Y. Wang, P. Deorani, K. Banerjee, N. Koirala, M. Brahlek, S. Oh, and H. Yang, Topological Surface States Originated Spin-Orbit Torques in Bi_2Se_3 , *Phys. Rev. Lett.* **114**, 257202 (2015).
- [15] D. Zhu, Y. Wang, S. Shi, K. Teo, Y. Wu, and H. Yang, Highly efficient charge-to-spin conversion from in situ $\text{Bi}_2\text{Se}_3/\text{Fe}$ heterostructures, *Appl. Phys. Lett.* **118**, 062403 (2021).
- [16] J. E. Moore, The birth of topological insulators, *Nature (London)* **464**, 194 (2010).
- [17] Y. Zhang *et al.*, Crossover of the three-dimensional topological insulator Bi_2Se_3 to the two-dimensional limit, *Nat. Phys.* **6**, 584 (2010).
- [18] S. Barua and K. P. Rajeev, Status of surface conduction in topological insulators, *AIP Adv.* **4**, 017135 (2014).
- [19] M. Dc *et al.*, Room-temperature high spin-orbit torque due to quantum confinement in sputtered $\text{Bi}_x\text{Se}_{(1-x)}$ films, *Nat. Mater.* **17**, 800 (2018).
- [20] M. DC, J.-Y. Chen, T. Peterson, P. Sahu, B. Ma, N. Mousavi, R. Harjani, and J.-P. Wang, Observation of high spin-to-charge conversion by sputtered bismuth selenide thin films at room temperature, *Nano Lett.* **19**, 4836 (2019).
- [21] M. Dc, T. Liu, J. Y. Chen, T. Peterson, P. Sahu, H. Li, Z. Zhao, M. Wu, and J. P. Wang, Room-temperature spin-to-charge conversion in sputtered bismuth selenide thin films via spin pumping from yttrium iron garnet, *Appl. Phys. Lett.* **114**, 102401 (2019).
- [22] Q. Lu, P. Li, Z. Guo, G. Dong, B. Peng, X. Zha, T. Min, Z. Zhou, and M. Liu, Giant tunable spin Hall angle in sputtered Bi_2Se_3 controlled by an electric field, *Nat. Commun.* **13**, 1650 (2022).
- [23] K. H. Han, Y. H. Park, J. U. Ahn, S. B. Kim, K. Kim, T. Park, O. Lee, B. Min, and H. C. Koo, Gate control of spin-orbit torque in a sputtered $\text{Bi}_2\text{Se}_3/\text{Ni}_{81}\text{Fe}_{19}$ device, *ACS Appl. Electron. Mater.* **5**, 2725 (2023).
- [24] A. R. Mellnik *et al.*, Spin-transfer torque generated by a topological insulator, *Nature (London)* **511**, 449 (2014).
- [25] J.-C. Rojas-Sánchez and A. Fert, Compared Efficiencies of Conversions between Charge and Spin Current by Spin-Orbit Interactions in Two- and Three-Dimensional Systems, *Phys. Rev. Appl.* **11**, 054049 (2019).
- [26] H. Wang, J. Kally, J. S. Lee, T. Liu, H. Chang, D. R. Hickey, K. A. Mkhoyan, M. Wu, A. Richardella, and N. Samarth, Surface-State-Dominated Spin-Charge Current Conversion in Topological-Insulator-Ferromagnetic-Insulator Heterostructures, *Phys. Rev. Lett.* **117**, 076601 (2016).
- [27] P. Deorani, J. Son, K. Banerjee, N. Koirala, M. Brahlek, S. Oh, and H. Yang, Observation of inverse spin Hall effect in bismuth selenide, *Phys. Rev. B* **90**, 094403 (2014).
- [28] C. H. Li, O. M. J. Van't Erve, J. T. Robinson, Y. Liu, L. Li, and B. T. Jonker, Electrical detection of charge-current-induced spin polarization due to spin-momentum locking in Bi_2Se_3 , *Nat. Nanotechnol.* **9**, 218 (2014).
- [29] L. Liu, A. Richardella, I. Garate, Y. Zhu, N. Samarth, and C.-T. Chen, Spin-polarized tunneling study of spin-momentum locking in topological insulators, *Phys. Rev. B* **91**, 235437 (2015).
- [30] L. A. Walsh, C. M. Smyth, A. T. Barton, Q. Wang, Z. Che, R. Yue, J. Kim, M. J. Kim, R. M. Wallace, and C. L. Hinkle, Interface chemistry of contact metals and ferromagnets on the topological insulator Bi_2Se_3 , *J. Phys. Chem. C* **121**, 23551 (2017).
- [31] W. Y. Choi *et al.*, All-electrical spin-to-charge conversion in sputtered $\text{Bi}_x\text{Se}_{(1-x)}$, *Nano Lett.* **22**, 7992 (2022).
- [32] K. Ferfolja, M. Fanetti, S. Gardonio, M. Panighel, I. Píš, S. Nappini, and M. Valant, A cryogenic solid-state reaction at the interface between Ti and the Bi_2Se_3 topological insulator, *J. Mater. Chem. C* **8**, 11492 (2020).
- [33] F. Bonell, M. Goto, G. Sauthier, J. F. Sierra, A. I. Figueroa, M. V. Costache, S. Miwa, Y. Suzuki, and S. O. Valenzuela, Control of spin-orbit torques by interface engineering in topological insulator heterostructures, *Nano Lett.* **20**, 5893 (2020).
- [34] I. C. Arango *et al.*, Spin-to-charge conversion by spin pumping in sputtered polycrystalline $\text{Bi}_x\text{Se}_{1-x}$, *Phys. Rev. Mater.* **7**, 075402 (2023).
- [35] E. Sagasta, Y. Omori, S. Vélez, R. Llopis, C. Tollan, A. Chuvilin, L. E. Hueso, M. Gradhand, Y. C. Otani, and F. Casanova, Unveiling the mechanisms of the spin Hall effect in Ta, *Phys. Rev. B* **98**, 060410(R) (2018).
- [36] E. Sagasta, Y. Omori, M. Isasa, Y. Otani, L. E. Hueso, and F. Casanova, Spin diffusion length of permalloy using spin absorption in lateral spin valves, *Appl. Phys. Lett.* **111**, 082407 (2017).
- [37] M. Isasa, E. Villamor, L. E. Hueso, M. Gradhand, and F. Casanova, Temperature dependence of spin diffusion length and spin Hall angle in Au and Pt, *Phys. Rev. B* **91**, 024402 (2015).
- [38] E. Sagasta, Y. Omori, M. Isasa, M. Gradhand, L. E. Hueso, Y. Niimi, Y. C. Otani, and F. Casanova, Tuning the spin Hall effect of Pt from the moderately dirty to the superclean regime, *Phys. Rev. B* **94**, 060412(R) (2016).
- [39] C. K. Safeer *et al.*, Large multidirectional spin-to-charge conversion in low-symmetry semimetal MoTe_2 at room temperature, *Nano Lett.* **19**, 8758 (2019).
- [40] See Supplemental Material at <http://link.aps.org/supplemental/10.1103/PhysRevB.108.104425> for details on the Cu growth (note S1), electrical characterization of Py, Cu, and BiSe (note S2), dependence of the spin signal on the interelectrode distance (note S3), 3D FEM simulation details to extract the interface resistance (note S4), Ti resistivity measurements (note S5), 3D FEM simulation to extract the spin diffusion length and the spin Hall angle of BiSe (notes S6 and S7, respectively), spin Hall measurement in a reference device as a control experiment (note S8), structural characterization of the LSV (note S9), and 3D FEM simulation to extract the spin diffusion length and spin Hall angle with different TiO_x resistivities (notes S10 and S11, respectively), which also includes Refs. [54–60].
- [41] F. Casanova, A. Sharoni, M. Erekhinsky, and I. K. Schuller, Control of spin injection by direct current in lateral spin valves, *Phys. Rev. B* **79**, 184415 (2009).

- [42] E. Villamor, M. Isasa, L. E. Hueso, and F. Casanova, Contribution of defects to the spin relaxation in copper nanowires, *Phys. Rev. B* **87**, 094417 (2013).
- [43] F. L. Bakker, A. Slachter, J.-P. Adam, and B. J. van Wees, Interplay of Peltier and Seebeck Effects in Nanoscale Nonlocal Spin Valves, *Phys. Rev. Lett.* **105**, 136601 (2010).
- [44] H. Isshiki, Z. Zhu, H. Mizuno, R. Uesugi, T. Higo, S. Nakatsuji, and Y. C. Otani, Determination of spin Hall angle in the Weyl ferromagnet Co_2MnGa by taking into account the thermoelectric contributions, *Phys. Rev. Mater.* **6**, 084411 (2022).
- [45] P. Jacquod, R. S. Whitney, J. Meair, and M. Büttiker, Onsager relations in coupled electric, thermoelectric, and spin transport: The tenfold way, *Phys. Rev. B* **86**, 155118 (2012).
- [46] V. T. Pham, H. Yang, W. Y. Choi, A. Marty, I. Groen, A. Chuvilin, F. S. Bergeret, L. E. Hueso, I. V. Tokatly, and F. Casanova, Large spin-charge interconversion induced by interfacial spin-orbit coupling in a highly conducting all-metallic system, *Phys. Rev. B* **104**, 184410 (2021).
- [47] H. L. Wang, C. H. Du, Y. Pu, R. Adur, P. C. Hammel, and F. Y. Yang, Scaling of Spin Hall Angle in 3d, 4d, and 5d Metals from $\text{Y}_3\text{Fe}_5\text{O}_{12}$ /Metal Spin Pumping, *Phys. Rev. Lett.* **112**, 197201 (2014).
- [48] W. Yan, E. Sagasta, M. Ribeiro, Y. Niimi, L. E. Hueso, and F. Casanova, Large room temperature spin-to-charge conversion signals in a few-layer graphene/Pt lateral heterostructure, *Nat. Commun.* **8**, 661 (2017).
- [49] H. He, L. Tai, D. Wu, H. Wu, A. Razavi, K. Wong, Y. Liu, and K. L. Wang, Enhancement of spin-to-charge conversion efficiency in topological insulators by interface engineering, *APL Mater.* **9**, 071104 (2021).
- [50] A. Soumyanarayanan, N. Reyren, A. Fert, and C. Panagopoulos, Emergent phenomena induced by spin-orbit coupling at surfaces and interfaces, *Nature (London)* **539**, 509 (2016).
- [51] J. C. Rojas-Sánchez, N. Reyren, P. Laczkowski, W. Savero, J. P. Attané, C. Deranlot, M. Jamet, J. M. George, L. Vila, and H. Jaffrès, Spin Pumping and Inverse Spin Hall Effect in Platinum: The Essential Role of Spin-Memory Loss at Metallic Interfaces, *Phys. Rev. Lett.* **112**, 106602 (2014).
- [52] W. Zhang, W. Han, X. Jiang, S. H. Yang, and S. S. P. Parkin, Role of transparency of platinum-ferromagnet interfaces in determining the intrinsic magnitude of the spin Hall effect, *Nat. Phys.* **11**, 496 (2015).
- [53] V. T. Pham, M. Cosset-Chéneau, A. Brenac, O. Boulle, A. Marty, J. P. Attané, and L. Vila, Evidence of interfacial asymmetric spin scattering at ferromagnet-Pt interfaces, *Phys. Rev. B* **103**, L201403 (2021).
- [54] H. Idzuchi, Y. Fukuma, and Y. Otani, Spin transport in non-magnetic nano-structures induced by non-local spin injection, *Phys. E (Amsterdam, Neth.)* **68**, 239 (2015).
- [55] P. Laczkowski *et al.*, Spin-dependent transport characterization in metallic lateral spin valves using one-dimensional and three-dimensional modeling, *Phys. Rev. B* **99**, 134436 (2019).
- [56] C. Geuzaine and J.-F. Remacle, Blossom-quad: A non-uniform quadrilateral mesh generator using a minimum-cost perfect-matching algorithm, *Int. J. Numer. Methods Eng.* **79**, 1309 (2009).
- [57] C. Geuzaine, GetDP: A general finite-element solver for the de rham complex, *Proc. Appl. Math. Mech.* **7**, 1010603 (2007).
- [58] R. J. Elliott, Theory of the effect of spin-orbit coupling on magnetic resonance in some semiconductors, *Phys. Rev.* **96**, 266 (1954).
- [59] Y. Yafet, *g factors and spin-lattice relaxation of conduction electrons*, in *Solid State Physics* (Academic Press, New York, 1963), Vol. 14, pp. 1–98.
- [60] C. Du, H. Wang, F. Yang, and P. C. Hammel, Systematic variation of spin-orbit coupling with *d*-orbital filling: Large inverse spin Hall effect in 3d transition metals, *Phys. Rev. B* **90**, 140407(R) (2014).